

Mixed-halide vacancy-ordered double perovskite for photovoltaic and photocatalysis applications

Sanika S. Padelkar,^{1,2,3,4} Vikram⁵, Jacek J. Jasieniak⁴, Alexandr N. Simonov², and Aftab Alam^{1,3,*}


¹Department of Physics, Indian Institute of Technology, Bombay, Powai, Mumbai 400076, India

²School of Chemistry, Monash University, Victoria 3800, Australia

³IITB-Monash Research Academy, IIT Bombay, Mumbai 400076, India

⁴Department of Materials Science & Engineering, Monash University, Victoria 3800, Australia

⁵Department of Materials, University of Oxford, Oxford OX1 3PH, United Kingdom

 (Received 4 June 2023; revised 4 February 2024; accepted 11 March 2024; published 17 April 2024)

Here, we report detailed first-principles calculations of the structural stability, optoelectronic properties, and interaction with water for a wide range of mixed-halide compositions of vacancy-ordered double perovskites $\text{Cs}_2\text{Pt}(\text{Cl}_x\text{I}_{1-x})_6$. Our calculations reveal that lower halide dopant levels subdue phase segregation and enhance the stability. $\text{Cs}_2\text{Pt}(\text{Cl}_x\text{I}_{1-x})_6$ demonstrate improved defect tolerance as compared to Cs_2PtI_6 due to the covalent nature of the Pt—X bond. The chloride-rich $\text{Cs}_2\text{Pt}(\text{Cl}_x\text{I}_{1-x})_6$ exhibit notably improved stability against reaction with water, far surpassing Cs_2PtI_6 due to the enhanced Cs—Cl bond strength and lower charge transfer between adsorbed H_2O and surface Cs atoms. The spectroscopic limited maximum photovoltaic efficiency for the optimal composition of $\text{Cs}_2\text{Pt}(\text{Cl}_{0.04}\text{I}_{0.96})_6$ under 1 sun AM1.5G is determined to be 24% for a 5- μm -thick film. Our calculations also suggest that the valence-band edge of this material might be positioned more positive than the standard potential of the oxygen-evolution reaction. These two factors combined with the high stability against reaction with water indicate that $\text{Cs}_2\text{Pt}(\text{Cl}_{0.04}\text{I}_{0.96})_6$ might be of considerable interest as a photovoltaic absorber, and possibly as a component of anodes for the photoelectrocatalytic water oxidation. Meanwhile, $\text{Cs}_2\text{Pt}(\text{Cl}_{0.96}\text{I}_{0.04})_6$ traverses relevant reduction and oxidation redox potentials, affirming it as a promising candidate for the overall photo(electro)catalyst water-splitting reaction.

DOI: [10.1103/PhysRevApplied.21.044031](https://doi.org/10.1103/PhysRevApplied.21.044031)

I. INTRODUCTION

Amongst the currently available renewable energy sources, solar irradiation is the most abundant on Earth. This has led to the rapid adoption of photovoltaics (PV) over the past decade, with silicon PVs dominating the market. To achieve cheaper, higher efficiency and/or lower embedded energy devices, alternative PV technologies are being actively developed, with the lead halide perovskite (LHP) solar cells emerging as one of the most exciting prospects [1,2]. While presenting a uniquely favorable combination of optoelectronic properties, LHPs are also subject to several well-established limitations, including toxicity of Pb^{2+} and limited stability in operation due to phase segregation and high susceptibility to moisture [3]. These challenges have been addressed to a certain extent through exploration of different variants of lead-free perovskites that can exhibit the defect tolerance of LHPs and high stability, for example, quasi-0D vacancy-ordered double perovskites (VODP) A_2BX_6 . The higher oxidation

state of the B cation in this class of compounds, e.g., Sn^{4+} in Cs_2SnI_6 , prevents material degradation and thereby imparts enhanced stability to the VODPs as compared to its three-dimensional (3D) counterparts, e.g. CsSnI_3 , in which the Sn^{2+} is prone to oxidation [4].

Hitherto, the A_2BX_6 compounds have predominantly been studied for applications in optoelectronic devices like light-emitting diodes, thermoelectric, scintillators, and high-resolution γ spectrometers on account of their high photoluminescence quantum yields (PLQY), [5–8] as well as promising moisture and thermal stability [9–15]. In the context of the PV applications, several iodine- and bromine-based VODP have been investigated, including experimental studies on $\text{Cs}_2\text{SnI}_4\text{Br}_2$, [16] Cs_2TiBr_6 , [17] Cs_2SnI_6 [18], and Cs_2PtI_6 [19]. The latter particularly holds a prominent position on account of its promising photoconversion efficiency (PCE) (ca. 14%), which is the highest amongst the double perovskite family [19]. To uphold these experimental observations, a theoretical study by Walkons *et al.* [20] concluded that Cs_2PtI_6 can be seen as a potential alternative to Pb-free perovskites owing to its suitable band gap, high charge-carrier

*Corresponding author. aftab@iitb.ac.in

mobility, high open-circuit voltage (V_{oc}), and short-circuit current-density (J_{sc}) values, as well as high PCE values as compared to other perovskite materials [20]. Moreover, Cs_2PtI_6 is reported as a suitable photoanode for photoelectrochemical (PEC) water oxidation with photocurrent of 0.8 mAcm^{-2} at 1.23 V [versus RHE (reversible hydrogen electrode)] under simulated AM1.5G sunlight [21]. Within a $BiVO_4/Cs_2PtI_6$ [22] heterojunction, an enhanced photocurrent of 0.92 mAcm^{-2} was achieved and could reach 2 mAcm^{-2} upon insertion of a IrO_x cocatalyst. Coupled with an optimal band-gap value (1.25 eV [21], 1.37 eV [23], and 1.4 eV [19]), high absorption coefficient, and appreciable PCE photocurrent, the Cs_2PtI_6 VODP compound exhibits better stability compared to other LHPs and lead-free perovskites upon exposure to ambient conditions [21,23]. Nevertheless, operational instability underpinned by phase segregation and high-moisture susceptibility persist. The later limitation to some extent has been addressed by the A_2BCl_6 [9,24] class of perovskites, by virtue of the chloride anions arguably playing a significant role in enhancing moisture stability. Although the A_2BCl_6 -based photovoltaics have not yet been extensively studied, the B-cation-doped chloride compounds [9,10,12,15,24–27] have been experimentally reported as luminescent materials with excellent moisture stability and also within light-conversion materials depicting excellent moisture stability.

Lately, the defect intolerance feature of A_2BX_6 systems has come forth in view of the interpretations led by Maughan *et al.* [28]. The defect tolerance versus intolerance is attributed to the degree of covalency of the B—X bond. For instance, the Te—I bond is more covalent than the Sn—I bond, hence increased covalency of the Te—I bond results in higher enthalpies of defect formation in Cs_2TeI_6 as compared to Cs_2SnI_6 , rendering the Cs_2TeI_6 to be defect intolerant. As compared to Cs_2SnI_6 and Cs_2TeI_6 , the Pt—I bond in the Cs_2PtI_6 system is indeed more covalent, suggesting that it might be defect intolerant. However, the Pt—Cl bond in Cs_2PtCl_6 is substantially less covalent than in Cs_2PtI_6 and Cs_2TeI_6 , and is comparable to the characteristics of the Sn—I bond in Cs_2SnI_6 . The decrease in covalency of the Pt—Cl bond is predominantly dictated by the electronegativity difference between Pt and halide, which is also evident in the case of Cs_2SnI_6 and Cs_2SnCl_6 . The defect concentration of Cs_2PtI_6 is reported to be approximately $2.5 \times 10^{12} \text{ cm}^{-3}$ [29] as compared to other VODPs like Cs_2SnI_6 , Cs_2SnCl_6 , which exhibit much larger defect densities (in the range approximately 10^{18} – 10^{21} cm^{-3}). As such, the extent of defect tolerance of the Cs_2PtI_6 and Cs_2PtCl_6 compounds as compared to other VODP or $MAPbI_3/FAPbI_3$ falls in a different ball park. Also Pt cation, in general, is experimentally reported to substantially increase the charge-carrier lifetime in comparison to Sn cations, which indicates that Pt helps in suppressing defects [30]. A device study simulation of both

the compounds suggests that even at moderate defect density levels of around 10^{17} cm^{-3} , Cs_2PtI_6 [31] performs far better with 23.5% PCE; whereas Cs_2SnI_6 with 10^{17} cm^{-3} defect densities [32] exhibits only 2.2% PCE. Hence, considering that both Cs_2PtI_6 and Cs_2PtCl_6 have significantly lower defect densities as compared to other state-of-the-art materials, we expect the covalency to get stronger as we move from Cs_2PtI_6 to Cs_2PtCl_6 . The defect transition energy level will vary accordingly, making Cs_2PtCl_6 relatively more defect tolerant than Cs_2PtI_6 .

Furthermore, Cs_2PtI_6 does in fact exhibit good transport properties, as can be concluded through the comparisons of the calculated effective carrier masses (m_e and m_h) against the well-studied Cs_2SnI_6 . In the latter case, the values are around $0.48m_0$ and $1.32m_0$, which are highly comparable to $0.51m_0$ and $1.45m_0$ for Cs_2PtI_6 [33]. Cs_2PtCl_6 has flatter valence bands as compared to Cs_2PtI_6 , which is expected to diminish the transport properties to some extent.

Thus, recognizing the limitations and advantages of both Cs_2PtI_6 (including lower defect tolerance and good transport properties) and Cs_2PtCl_6 (including high defect tolerance and suppressed transport), our work aims to explore if these can be addressed through mixing of halides in an optimal manner. Besides, the coalescence of Cs_2PtI_6 having excellent PCE and distinctly stable Cs_2PtCl_6 expedites a potential approach towards emerging lead-free perovskites with improved moisture stability. Previous reports on the effects of introduction of Cl^- into VODPs [34,35] for enhancing stability and inhibiting defects have majorly focused on high concentrations of chloride, ranging from 25 at. % to 75 at. %, which hampers the optical performance. The latter limitation might be overcome at lower levels of Cl^- doping in VODPs, which are yet to be explored.

Herein, we have undertaken a computational study of the $Cs_2Pt(Cl_xI_{1-x})_6$ system to explore the effects of halide anion mixing (in a full x range from 0 to 100 at. %) on the properties of this promising class of materials. The apparent fragility of the perovskite family, especially mixed-halide perovskites is the phase segregation, which arises on account of halide ion migration. This demixing of the halides into separate phases triggers the operational instability. One of the models unravelling the origin of halide migration is based on thermodynamic stabilization. Under thermodynamic equilibrium assumption, the detailed thermodynamical phase-diagram analysis to some extent assists in predicting a range of chloride concentrations that can lead to either phase segregation or homogeneous distribution of halide anions when Cl^- is doped and alloyed in Cs_2PtI_6 . The thermodynamic chemical stability, optoelectronic properties, charge disproportion, and the moisture stability are scrutinised for the identified homogeneously mixed compounds. Based on these insights, we propose a composition that presents an

optimal combination of the key characteristics for photovoltaic and photo(electro)catalytic applications.

II. COMPUTATIONAL DETAILS

Ab initio calculations were performed using the projector-augmented wave (PAW) method within the density functional theory (DFT) as implemented in the Vienna *ab initio* simulation package (VASP) [36]. The plane-wave cut-off energy was set to 520 eV. For the exchange-correlational term, SCAN meta-GGA functional was used for all the electronic structure and surface calculations. PAW potentials Cs($5s^25p^66s^1$), Pt($6s^15d^9$), I($5s^25p^5$), and Cl($3s^23p^5$) were used for all calculations.

For all pristine and mixed-halide systems with 2 at. % <math>x < 98</math> at. %, a conventional unit cell consisting of 36 atoms was used. For mixed-halide systems with $x = 2$ and 98 at. %, a $2 \times 2 \times 2$ supercell was employed. Ionic relaxation was performed using the conjugate gradient algorithm. The atomic positions were optimized until residual forces on each atom were less than $0.001 \text{ eV \AA}^{-1}$, while the tolerance value for energy optimization was kept as 10^{-6} eV . For optical and electronic calculations, a Γ -centred k -point mesh with density of $2\pi \times 0.01 \text{ \AA}^{-1}$ was selected to sample the Brillouin zone (BZ) using the tetrahedron method. Effective band structures of the parent and I/Cl mixed conventional unit cells unfolded onto the primitive cell were evaluated using the BandUp code [37,38].

The optical properties for all the systems were simulated by including explicit electron-hole interactions solving the Bethe-Salpeter equation (BSE) [39,40] on top of single-shot GW calculations (G_0W_0 +BSE method). Additional details on G_0W_0 +BSE calculations are provided in the Supplemental Material [41]; also see Refs. [19,21,23, 42–46]. The optical transition probabilities were calculated from the dipole-dipole transition matrix elements. An improved version over Shockley-Queisser (SQ) efficiency limit called spectroscopic limited maximum efficiency (SLME), as proposed by Yu and Zunger [47], was calculated as a figure of merit to evaluate photovoltaic performance. The chemical phase diagrams for all the pristine and mixed-halide systems were plotted using the Chesta code [48] by calculating the formation energies of the target compound and its corresponding secondary phases.

The surfaces of Cs_2PtI_6 and Cs_2PtCl_6 were simulated using a slab model, with a vacuum of 15 Å. A $4 \times 4 \times 1 k$ mesh was used for the BZ integration of all surface slabs. For all surface-related calculations involving bare surfaces as well as surface/ H_2O interfaces, van der Waals correction was taken into consideration. Further surface calculation details are included in the Supplemental Material [41]. Bader charge analysis for bulk and surface slabs was performed using Bader code [49] from the Henkelman's Group. The electrostatic potential of the (111) surface was

calculated to obtain external vacuum level, which was used as a reference level for the band energy-level calculations and Cs 1s level was selected as the representative core level. The absolute valence (VBM) and conduction-band maximum (CBM) energy levels (E_{VBM} and E_{CBM}) were calculated using the following formulae:

$$E_{\text{VBM}} = \epsilon_{\text{VBM}}^{\text{KS}} - [E_{\text{Cs-1s}}^{\text{bulk}} + E_{\text{Cs-1s}}^{\text{surf}}] - V_{\text{vacuum}}, \quad (1)$$

where $\epsilon_{\text{VBM}}^{\text{KS}}$ and $\epsilon_{\text{CBM}}^{\text{KS}}$ are the Kohn-Sham (KS) eigenvalues corresponding to VBM and CBM levels in the bulk phase, $E_{\text{Cs-1s}}^{\text{bulk}}$ and $E_{\text{Cs-1s}}^{\text{surf}}$ are the average Cs 1s core-level energies in the bulk and innermost layers of the surface slab, respectively, and V_{vacuum} is the vacuum energy estimated from the planar average electrostatic potential calculations.

III. RESULTS AND DISCUSSION

A. Stability of pristine and mixed-halide systems

The pristine vacancy-ordered double perovskites Cs_2PtCl_6 and Cs_2PtI_6 crystallize as face-centred cubic structures with a space group $Fm\bar{3}m$ (225) [19,21,42,50]. Figure 1 shows a conventional cubic unit cell of pristine (left) and mixed-halide (right) VODPs, where Cs atoms reside at $8c(1/4, 1/4, 1/4)$, Pt atoms at $4a(0, 0, 0)$, and halide anions at $24e(x, 0, 0)$ Wyckoff sites. The corresponding optimized lattice parameters for both pristine and mixed-halide systems are presented in Table S1 within the Supplemental Material [41]. The relaxed lattice constants (11.77 \AA for Cs_2PtI_6 and 10.57 \AA for Cs_2PtCl_6) calculated herein are in a good agreement with previous experimental (11.37 \AA for Cs_2PtI_6 [43] and 10.19 \AA for Cs_2PtCl_6 [42]) and theoretical studies (11.77 \AA for Cs_2PtI_6 and 10.62 \AA for Cs_2PtCl_6) [44]. As expected, the lattice parameter decreases with increasing the concentration of chlorine in $\text{Cs}_2\text{Pt}(\text{Cl}_x\text{I}_{1-x})_6$.

The structural stability of the materials was assessed using Goldschmidt's tolerance factor:

$$\tau = \frac{R_{\text{Cs}} + xR_{\text{Cl}} + (1-x)R_{\text{I}}}{\sqrt{2}(R_{\text{Pt}} + xR_{\text{Cl}} + (1-x)R_{\text{I}})}, \quad (2)$$

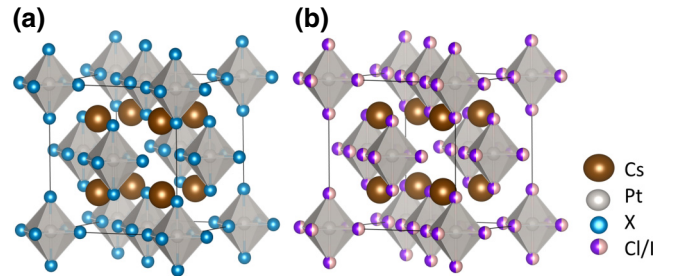


FIG. 1. Crystal structure of (a) pristine $\text{Cs}_2\text{PtCl}_6/\text{Cs}_2\text{PtI}_6$, and (b) mixed-halide $\text{Cs}_2\text{Pt}(\text{Cl}_x\text{I}_{1-x})_6$ perovskites.

where R_{Cs} , R_{Pt} , R_{Cl} , and R_{I} are the ionic radii of Cs^+ (1.67 Å), Pt^{4+} (0.62 Å), Cl^- (1.81 Å), and I^- (2.2 Å), respectively. All $\text{Cs}_2\text{Pt}(\text{Cl}_x\text{I}_{1-x})_6$ compounds examined herein exhibit tolerance factors close to 1 ($\tau = 0.97\text{--}1.01$ range), indicating the highly symmetrical and stable cubic structure (Table S13 within the Supplemental Material [41]). Goldschmidt's criterion is purely geometric and often omits the chemistry (electronegativity, charge, etc.) mediated stability of the compound under consideration. In order to check the said stability, we have simulated the thermodynamical phase diagrams of all $\text{Cs}_2\text{Pt}(\text{Cl}_x\text{I}_{1-x})_6$ systems examined herein.

To investigate the thermodynamic stability and range of chemical potentials favorable for the formation of the target compounds, the formation energy of $\text{Cs}_2\text{Pt}(\text{Cl}_x\text{I}_{1-x})_6$ and all corresponding secondary phases were simulated using the GGA-PBE functional [51]. This approach enables prediction of the chemical environment and conditions necessary for the synthesis of a multicomponent material. The extent of the stability region within the chemical potential space determines the possibility of the formation of the target system, relative to the formation of simpler, secondary phases. All the possible competing secondary phases are obtained from the ICSD material database [52]. They are as follows: Cs_2I_8 , CsI_3 , CsI , Cs_3I , Cs_2Pt , Cs_3Pt , PtI_2 , PtI_3 , PtI_4 , Pt_2I_6 , Pt_3I_8 , Cs_2PtCl_4 , CsCl , ICl , ICl_3 , CsICl_2 , PtCl_3 , PtCl_4 and PtCl_2 . The constraint equations for each of the target phases Cs_2PtI_6 , $\text{Cs}_2\text{Pt}(\text{Cl}_{0.02}\text{I}_{0.98})_6$, $\text{Cs}_2\text{Pt}(\text{Cl}_{0.04}\text{I}_{0.96})_6$, $\text{Cs}_2\text{Pt}(\text{Cl}_{0.08}\text{I}_{0.92})_6$, $\text{Cs}_2\text{Pt}(\text{Cl}_{0.12}\text{I}_{0.88})_6$, $\text{Cs}_2\text{Pt}(\text{Cl}_{0.25}\text{I}_{0.75})_6$, $\text{Cs}_2\text{Pt}(\text{Cl}_{0.5}\text{I}_{0.5})_6$, $\text{Cs}_2\text{Pt}(\text{Cl}_{0.75}\text{I}_{0.25})_6$, $\text{Cs}_2\text{Pt}(\text{Cl}_{0.88}\text{I}_{0.12})_6$, $\text{Cs}_2\text{Pt}(\text{Cl}_{0.92}\text{I}_{0.08})_6$, $\text{Cs}_2\text{Pt}(\text{Cl}_{0.96}\text{I}_{0.04})_6$, $\text{Cs}_2\text{Pt}(\text{Cl}_{0.98}\text{I}_{0.02})_6$, Cs_2PtCl_6 and competing secondary phases are plotted in their respective chemical phase diagrams shown in Fig. 2. The extent of the stability region varies with Cl concentrations (x). Higher stability was expectedly found for Cs_2PtCl_6 and Cs_2PtI_6 materials, as well as for a range of mixed-halide $\text{Cs}_2\text{Pt}(\text{Cl}_x\text{I}_{1-x})_6$ perovskites with $x \leq 12$ at. % and $x \geq 92$ at. % [see Figs. 2(a)–2(i)]. However, compositions with $x = 25, 50, 75, 88$ at. % exhibited very limited regions of stability and were predicted to preferably co-exist with other secondary phases [see Figs. 2(j)–2(m)]. Extended discussions of the thermodynamic chemical stability [46] are provided in Sec. S2 within the Supplemental Material [41]. Table S4 within the Supplemental Material [41] gives the range of chemical potentials required to synthesize each of the target systems in a single phase.

A similar stability trend is also observed experimentally in another compound belonging to the same class, i.e., $\text{Cs}_2\text{Sn}(\text{I}_x\text{Cl}_{1-x})_6$, reported by Zhu *et al.*, where only 2.15%, 3.17%, 3.67%, 4%, 8%, 15%, and 86% I-mixed Cs_2SnCl_6 were found to be experimentally stable [53]. A peculiar limitation to the incorporation of iodine replacing chlorine atoms was highlighted. Multiple phase formation

in the mixed-halide system was reported at intermediate iodine concentrations. This limitation can intuitively be attributed to the difference in the ionic radii of halogens, i.e., Cl^- (1.81 Å) < Br^- (1.96 Å) < I^- (2.2 Å). This indicates that incorporation of the Br^- in Cs_2SnI_6 is relatively easier as compared to Cl^- atom. However, it is worthwhile to emphasize that the chemical phase-stability calculations are performed under thermodynamic equilibrium. It is expected that due to the effect of higher temperature, entropic term $T\Delta_{\text{mix}}(x)$ increases leading to a higher thermodynamic stability of the mixed-phase composition. Hence, there is indeed a likelihood for the formation of $\text{Cs}_2\text{Pt}(\text{Cl}_x\text{I}_{1-x})_6$ (where, $x = 25, 50, 75, 88$ at. %) in an ordered state or possibly disordered state due to the configurational disorder arising out of halide mixing; this is further discussed using free enthalpy of mixing in Sec. B. Nevertheless, our further study on optoelectronic and stability against reaction with water in this paper will be focused on $\text{Cs}_2\text{Pt}(\text{Cl}_x\text{I}_{1-x})_6$ (where, $x = 2, 4, 8, 12, 92, 96, 98$ at. %). This is done mainly to promote competent systems amongst these as promising photovoltaic absorbers and photocatalysts exhibiting enhanced stability.

B. Electronic structure and Gibbs free energy

Experimental band gaps reported for Cs_2PtX_6 ($X = \text{Cl}, \text{Br}, \text{I}$) have been controversial. Table I shows the experimental and our calculated band-gap values simulated at different exchange correlation functional levels. The experimental band gap of Cs_2PtI_6 is reported to be 1.25 eV [21], 1.37 eV [23], and 1.4 eV [19] depending on the synthesis processes and the corresponding samples. Whereas, Cs_2PtCl_6 shows an even larger difference in the experimentally reported band gaps (2.16 eV by Hamdan *et al.* [42] and 2.90 eV by Wu *et al.* [45]). As evident, our simulated band-gap values do not corroborate well with the experimental reports. The inconsistency is more significant in Cs_2PtCl_6 where the HSE06 band gap is 3.44 eV (also consistent with other DFT work [54]). In contrast, the HSE06 band gap of Cs_2PtI_6 , 1.44 eV (also consistent with other DFT reports [54,55]), is comparatively closer to experimental values. Keeping in mind the said discrepancy between theoretical and experimental band-gap values, it is imperative to select an appropriate exchange correlation functional, which can yield the experimental band gap of both the systems within a reasonable range. This is more useful for a reliable theoretical prediction of band-gap values for the mixed systems $\text{Cs}_2\text{Pt}(\text{Cl}_x\text{I}_{1-x})_6$, where no experimental reports are available. Although, the PBE functional predicts the band gap of Cs_2PtCl_6 close to one of the experiments [42], the Cs_2PtI_6 band gap is highly underestimated. In contrast, though the standard HSE06 functional severely overestimates Cs_2PtCl_6 band-gap value, the HSE06 band gap of Cs_2PtI_6 lies within a

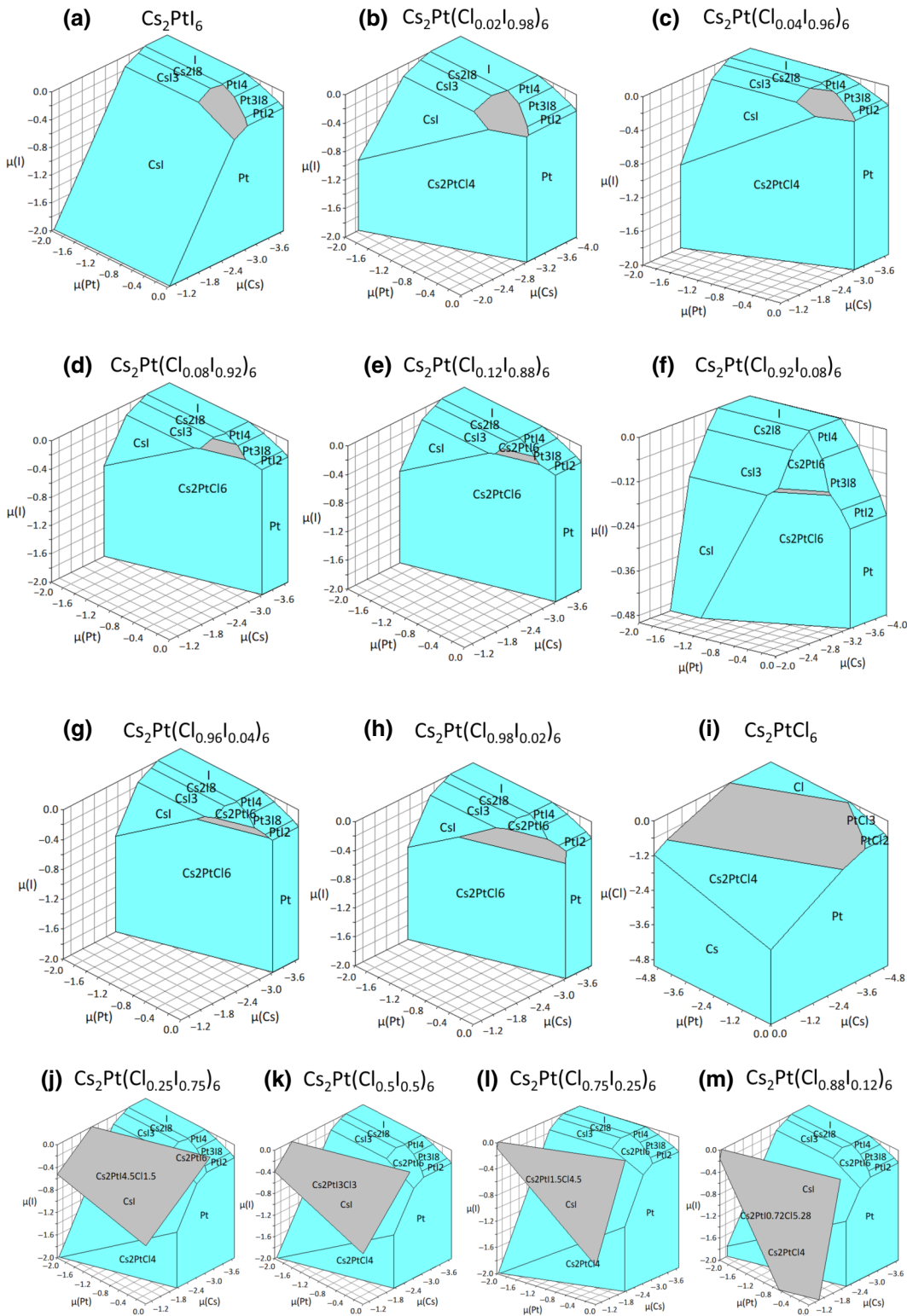


FIG. 2. (a)–(i) Chemical phase diagrams of pristine and mixed-halide systems, which are stable in single phase, (a) Cs_2PtI_6 , (b) $\text{Cs}_2\text{Pt}(\text{Cl}_{0.02}\text{I}_{0.98})_6$, (c) $\text{Cs}_2\text{Pt}(\text{Cl}_{0.04}\text{I}_{0.96})_6$, (d) $\text{Cs}_2\text{Pt}(\text{Cl}_{0.08}\text{I}_{0.92})_6$, (e) $\text{Cs}_2\text{Pt}(\text{Cl}_{0.12}\text{I}_{0.88})_6$, (f) $\text{Cs}_2\text{Pt}(\text{Cl}_{0.92}\text{I}_{0.08})_6$, (g) $\text{Cs}_2\text{Pt}(\text{Cl}_{0.96}\text{I}_{0.04})_6$, (h) $\text{Cs}_2\text{Pt}(\text{Cl}_{0.98}\text{I}_{0.02})_6$, and (i) Cs_2PtCl_6 . The grey shaded region represents the stability region of target system. (j) $\text{Cs}_2\text{Pt}(\text{Cl}_{0.25}\text{I}_{0.75})_6$, (k) $\text{Cs}_2\text{Pt}(\text{Cl}_{0.5}\text{I}_{0.5})_6$, (l) $\text{Cs}_2\text{Pt}(\text{Cl}_{0.75}\text{I}_{0.25})_6$, (m) $\text{Cs}_2\text{Pt}(\text{Cl}_{0.88}\text{I}_{0.12})_6$. The grey shaded region in these four diagrams are the projected phase diagrams showing co-existence of target phases with other secondary phases (i.e., multiple phase formation).

TABLE I. Calculated band gap of Cs₂PtI₆ and Cs₂PtCl₆ using different exchange correlation functionals. Experimental values are given for comparison.

System	PBE (eV)	PBE+SOC (eV)	HSE (eV)	HSE+SOC (eV)	SCAN (eV)	SCAN+SOC (eV)	Experiment (eV)
Cs ₂ PtI ₆	0.68	0.55	1.44	1.30	0.94	0.93	1.25 [21], 1.37 [23], 1.40 [19]
Cs ₂ PtCl ₆	2.1	1.83	3.44	3.28	2.40	2.37	2.16 [42], 2.90 [45]

reasonable range as compared to available experimental data. The inclusion of spin-orbit coupling (SOC) effects as well cannot resolve the band-gap deviation with respect to experimental values (see Table I).

The meta-GGA SCAN (strongly constrained and appropriately normed) functional is known to accurately capture different types of bonding, as well as van der Waals interactions with a much lower computational cost and no empirical parameters, unlike the HSE06 functional [56]. In order to capture a reliable trend of band gap versus halide-mixing composition, we opt for the SCAN functional, which is expected to perform better in addressing the chemical bonding, which are crucial in stabilizing the mixed-halide compounds. We found that the overall relative trend of band gap remains almost similar irrespective of the type of functional used, except their magnitude.

Using the meta-GGA SCAN functional, we ascertain that Cs₂PtI₆ exhibits an indirect band gap from Γ to X, whereas Cs₂PtCl₆ shows a direct band gap at the Γ point as observed from the unfolded (effective) band structure shown in Fig. 3(iii) (right panel). Experimentally, Cs₂PtI₆ [19,21] is confirmed to be an indirect band-gap semiconductor, which is consistent with our findings. The meta-GGA SCAN band gap for Cs₂PtI₆ is 0.93 eV, which is underestimated, while that of Cs₂PtCl₆ (2.4 eV) lies in an acceptable range with respect to the experimentally reported range of band-gap values. The CBM is mainly derived from the antibonding states of Pt-5d- e_g and I-5p/Cl-3p orbitals. The VBM of Cs₂PtI₆ consists of the nonbonding I-5p orbitals, while the VBM of Cs₂PtCl₆ shows hybridization between Pt-5d- t_{2g} and Cl-3p orbitals. As expected, the d orbital of Pt splits into twofold degenerate e_g states and threefold degenerate t_{2g} states. The Pt-5d- e_g states contribute to the CBM hybridizing with I-5p states, whereas the Pt-5d- t_{2g} states are situated near the VBM. Projected density of states (PDOS) [Figs. 3(a-ii), 3(b-ii)] for both the systems indicate a similar nature of Pt and halide states, which are spread around the same energy range, whereas the Cs states are localized. Cs⁺ and PtX₆²⁻ octahedral complex acquire ionic interaction. Though Cs cations do not contribute much to the valence band, with its 6s electrons being donated to Pt—X hybrid orbitals, leaving the Cs 6s states empty in the valence band. Unlike many Cl-based VODPs, e.g., Cs₂SnCl₆, which has a higher band-gap value of 3.5 eV, few VODPs

show reduced band-gap values, viz., Cs₂PdCl₆, Cs₂PbCl₆, Cs₂GeCl₆, Cs₂PtCl₆. Cs₂PtCl₆ also belongs to the latter with a reduced band gap. Based on our theoretical results, this reduction is attributed to the band-edge orbital contributions. The simulated PDOS of Cs₂PtCl₆ in Fig. S1 within the Supplemental Material [41] shows slight presence of Pt-5s near the band edge levels leading to s -orbital overlapping, which is not evident in the PDOS of Cs₂PtI₆. The rise of Pt-5s orbitals at the VBM leads to larger overlap, thus reducing the band gap of Cs₂PtCl₆ to 2.4 eV in comparison to other Cl-based compounds exhibiting band gap > 3.5 eV. The splitting of the Pt-5d orbital into Pt-5d- e_g at CBM and Pt-5d- t_{2g} at VBM indicates that the band gap is dictated by the intra-atomic d - d transitions for Cs₂PtCl₆. This is in contrast to Cs₂PtI₆, for which the band gap arises purely from I-5p and Pt-5d- e_g orbitals. Additionally, chemical bonding analysis of Cs₂PtCl₆ and Cs₂SnCl₆ suggests how the Pt—X bonding nature can affect the magnitude of band gap. As reported in previous studies, the B—X bond in perovskite systems is best described as an ionic-covalent bond [57]. Along the same lines, as seen from deformation density difference maps and contour maps of Cs₂PtI₆, Cs₂PtCl₆, and Cs₂SnCl₆ (see Fig. S3 within the Supplemental Material [41]), the ionic character in Sn—Cl bonds of Cs₂SnCl₆ is higher. While the Pt—Cl bond in Cs₂PtCl₆ is more covalent in nature. The strong covalent nature is often responsible for the reduction in band gap. Instinctively, partial replacement of I by Cl is expected to raise the band gap due to the increase of electronegativity difference between B-site element ($\chi_{\text{Pt}} = 2.28$) and halide ions ($\chi_{\text{I}} = 2.66$ and $\chi_{\text{Cl}} = 3.16$). The smaller the electronegativity difference, the stronger is the Pt—X covalent bonding, making the valence band more dispersive, which is evident in the case of Cs₂PtI₆. This, in turn, makes the VBM higher in energy resulting in a smaller band gap for Cs₂PtI₆. On the other hand, in the case of Cs₂PtCl₆, the VBM bands are flatter resulting in a lower mobility of holes as compared to Cs₂PtI₆. The band topology thus clearly indicates that the optoelectronic performance of Cs₂PtCl₆ will be significantly hindered as compared to Cs₂PtI₆. Although complete replacement by the Cl⁻ atoms may impart good overall stability to the system [58], the optical performance may not be appreciable due to the blue shift in the visible spectrum [Fig. 5(a)].

The electronic band structure and atom and orbital projected density of states for all chemically phase stable

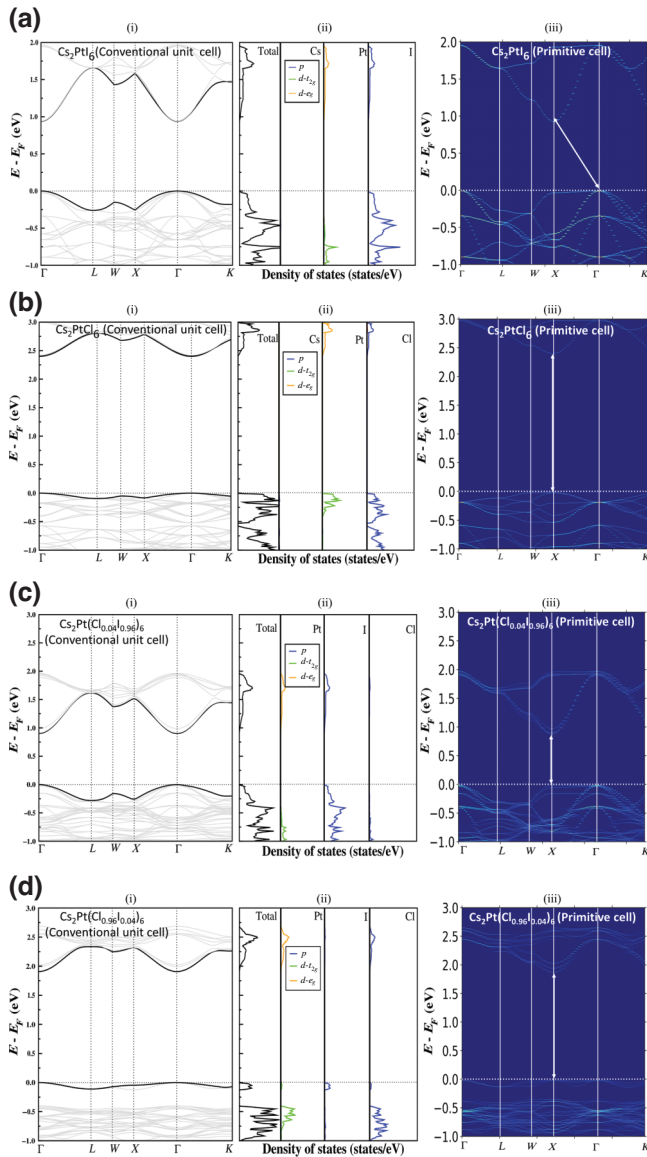


FIG. 3. (i,ii) Simulated band structure and density of states using conventional unit cell (iii) unfolded band structure in the primitive unit cell for (a) Cs_2PtI_6 , (b) Cs_2PtCl_6 , (c) $\text{Cs}_2\text{Pt}(\text{Cl}_{0.04}\text{I}_{0.96})_6$, and (d) $\text{Cs}_2\text{Pt}(\text{Cl}_{0.96}\text{I}_{0.04})_6$, respectively, using SCAN functional.

mixed halide $\text{Cs}_2\text{Pt}(\text{Cl}_x\text{I}_{1-x})_6$ systems are shown in Fig. S1 within the Supplemental Material [41]. Due to the Pt—X hybridized nature of the valence-band edges, substitution of halides is expected to majorly impact the valence-band levels. Here, we have considered two representative mixed-halide cases ($x = 4$ at. % and 96 at. % Cl) to discuss the overall evolution of band topology and band gap. In the case of 4 at. % Cl-mixed-halide system $\text{Cs}_2\text{Pt}(\text{Cl}_{0.04}\text{I}_{0.96})_6$ [Fig. 3(c)], the Cl-mediated bands lie deep inside the VB due to the lower energy of $3p$ orbitals of the Cl dopant as compared to the $5p$ orbitals of the I atoms. This is

confirmed by PDOS calculations where the Cl energy levels are localized quite below the valence-band edge. From the 96 at. % Cl-mixed $\text{Cs}_2\text{Pt}(\text{Cl}_{0.96}\text{I}_{0.04})_6$ PDOS plot [Fig. 3(d)], it can be seen that the I- $5p$ states are contributing to the VBM, which is isolated from the intermediate valence bands by 0.2–0.3 eV. Although, a distinct feature of the vacancy-ordered double perovskite band structure is the appreciable gap between topmost valence bands and deeper bands, which is visible at the 1.5–2 eV energy level, reflecting the isolated octahedral framework of quasi-0D perovskite. But this new gap emerging between VBM and intermediate valence bands in 96 at. % Cl-mixed $\text{Cs}_2\text{Pt}(\text{Cl}_{0.96}\text{I}_{0.04})_6$ system is unprecedented. Such a gap is noticeable for 88 at. % $\leq x \leq 98$ at. % Cl-mixed systems as well. This gap originates from the distorted octahedral shape and chemical environment present in this composition range as the chloride and iodine atoms are not uniformly distributed throughout the crystal. This imbalance of distortion and retention of the octahedral shape and chemical environment (Pt—I and Pt—Cl) throughout the lattice sets off a disproportion in the electronic band structure as well. This claim comes from the fact that the VBM in these cases are exceedingly contributed by I- $5p$ orbital and Pt- $5d$ orbital (in particular from the Pt atom, which is a part of the octahedra where I and Cl are both present simultaneously). However, such disproportionate gap does not appear for lower chloride compositions, i.e., 2 at. % $\leq x \leq 12$ at. %. For instance, 4 at. % Cl-mixed system electronic structure [Fig. 3(c)] depicts continuous valence bands without any abrupt gap. Although the octahedral shape and nature is distorted in this case too, unlike 96 at. % Cl-mixed $\text{Cs}_2\text{Pt}(\text{Cl}_{0.96}\text{I}_{0.04})_6$ system, the distortion is significantly weaker. Moreover, the charge transfer between Pt—Cl bond is not significantly affecting the Pt—I bond strength on the same octahedron as well as other octahedra. Whereas, the distortion of octahedra in $\text{Cs}_2\text{Pt}(\text{Cl}_{0.96}\text{I}_{0.04})_6$ is quite notable and the Pt—I charge transfer is stronger. The charge around Pt bonded with one iodine and five chloride ions is appreciably altered as compared to the Pt atoms surrounded by all six chloride atoms. This difference in environment around Pt atom on the I-substituted octahedron leads to hybridization of Pt—I and Pt—Cl with major contribution from iodide, which has its energy level I- $3p$ lying above Cl- $5p$ and hence the discrete gap arises owing to this orbital-energy level difference. The simulated band gaps and their respective nature for mixed-halide systems using meta-GGA SCAN functional are shown in Table S6 within the Supplemental Material [41]. Figure 4(a) shows the Cl concentration dependence of band gap value, which clearly deviates from what is expected from Vegard’s law. Instead, an unconventional band-gap bowing is observed, where for a particular Cl concentration the band-gap value is lower than those for the two pristine end compounds. The band-gap nonlinearity is expressed using the following equation:

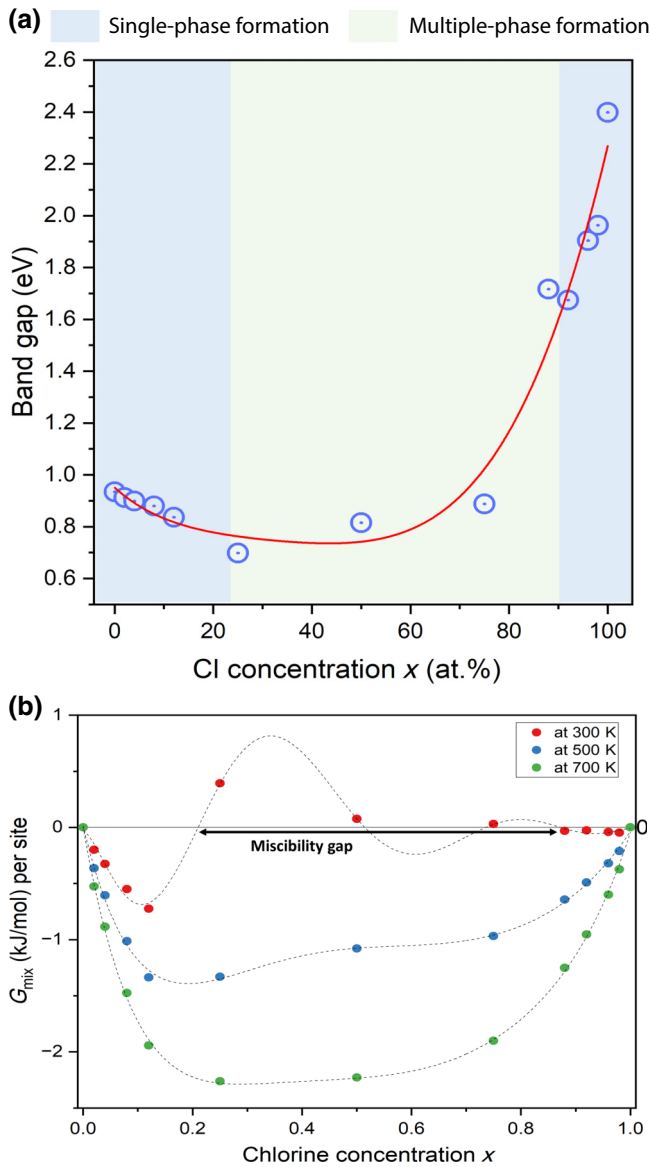


FIG. 4. (a) Simulated band gap versus Cl concentrations x (at. %) in $\text{Cs}_2\text{Pt}(\text{Cl}_x\text{I}_{1-x})_6$. (b) Free enthalpy of mixing versus Cl concentrations x (at. %) in $\text{Cs}_2\text{Pt}(\text{Cl}_x\text{I}_{1-x})_6$.

$$E_g(\text{Cs}_2\text{PtCl}_x\text{I}_{1-x}) = E_g(\text{Cs}_2\text{PtI}_6) + E_g(\text{Cs}_2\text{PtCl}_6) - bx(1-x), \quad (3)$$

where the bowing parameter, b is 1.46. The band-gap bowing phenomenon is majorly reported across various mixed-halide or B-doping perovskite (single, double, layered) system [28,59–63]. We inspected the possibility of any structural distortions by considering the variation of unit cell volume (V) as a function of Cl concentration (x) (Fig. S2 within the Supplemental Material [41]). The V versus x trend is fairly linear between $x = 0$ and $x = 0.75$; with a slight nonlinearity between $x = 0.75$ and $x = 0.88$. The bond lengths between different neighboring pairs

shows a similar jump. The abrupt change in band gap between $x = 0.75$ and $x = 0.88$ can be attributed to this. The band gap versus x trend [Fig. 4(a)] almost remains the same irrespective of the unit-cell size taken for simulation for different x . The emergence of this band-gap bowing phenomenon can be attributed to several reasons: (1) volume deformation potential effects—this typically arises from the electronic structure changes in the pristine compound as a consequence of the volumetric changes due to substitutional doping; (2) chemical effects—this is due to the intermixing of atomic orbitals at different energy levels; and (3) broken symmetry—typically the pristine Cs_2BX_6 compounds crystallize in $Fm\bar{3}m$ (225) space group having centrosymmetric point groups with center of inversion at B atom. For each of these pristine halide compounds, the VBM to CBM transition is forbidden due to the inversion symmetry. However, upon replacing the parent halogen, say I by Cl, there is a reduction of symmetry (center of inversion absent) and change in coordination of B atom. As a direct consequence of this, the fundamental band gap becomes optically allowed. This has been observed experimentally for the $\text{Cs}_2\text{Sn}(\text{Br}_x\text{Cl}_{1-x})_6$ system [60]. Figure S6 within the Supplemental Material [41] shows the electronic band structure and the dipole-dipole transition probability for Cs_2PtI_6 and Cs_2PtCl_6 and $\text{Cs}_2\text{Pt}(\text{Cl}_x\text{I}_{1-x})_6$ (where, $x = 2, 4, 8, 12, 92, 96, 98$ at. %). For Cs_2PtCl_6 and Cs_2PtI_6 , the fundamental band gap is symmetry disallowed, while for mixed-halide systems $\text{Cs}_2\text{Pt}(\text{Cl}_x\text{I}_{1-x})_6$ ($x = 8$ at. %, 12 at. %, 25 at. %) it is symmetry allowed. This indicates that the band-gap decrement for mixed-halide systems $\text{Cs}_2\text{Pt}(\text{Cl}_x\text{I}_{1-x})_6$ ($x = 8$ at. %, 12 at. %, 25 at. %) might be a consequence of the broken symmetry for these Cl concentrations, which indeed changes the coordination of the Pt atoms due to the octahedral distortion. While the reason for anomalous (dual) band-gap bowing (at $x = 25$ at. % and $x = 75$ at. %) may also be related to the multiple phase formation in the intermediate mixed-halide compositions ($x = 25$ at. %, 50 at. %, 75 at. %, and 88 at. %), as suggested by our chemical phase-stability analysis. Such a nonlinear band-gap trend across varying halide and/or B-cation concentrations has been reported for $\text{Cs}_2\text{Sn}(\text{Cl}_x\text{I}_{1-x})_6$ [53] and triple halide lead-based perovskites [2]. Both the studies suggest a nonlinear trend in the band gap at particular compositions, which were experimentally observed to show multiple phases and/or phase segregation. Interestingly, in our present case, the anomalous band bowing [Fig. 4(a)] occurs over a range of compositions ($x = 25$ at. %, 50 at. %, 75 at. %, and 88 at. %) that are predicted to be unstable as per our chemical phase-stability calculations. This instability range $25 \text{ at. \%} \leq x \leq 88 \text{ at. \%}$ resembles the miscibility gap observed in mixed-halide systems that are prone to phase segregation due to halide-ion migration. The miscibility gap indicated in free enthalpy of mixing G_{mix} plot shown in Fig. 4(b) is consistent with our interpretations

based on chemical phase-stability analysis. The unstable mixed-halide phases that are prone to phase segregate at room temperature can be stabilized in single phase by tuning the synthesis temperature to 500–700 K as shown in Fig. 4(b).

C. Optoelectronic properties

Vacancy-ordered double perovskites are proclaimed to show strong excitonic effects, e.g., Cs_2TiCl_6 , which exhibits a large exciton binding energy [64]. This led us to explore if the inclusion of excitonic effects in our calculations may explain the deviations of our computed band gaps from the experiments, particularly in the case of Cs_2PtCl_6 . In order to cross-check this, the absorption coefficients for the four shortlisted systems (Fig. 3) were simulated using the G_0W_0 +BSE method to examine the role of exciton interactions with varying Cl concentration. This is shown in Fig. 5(a). The difference in the absorption spectrum of I-rich and Cl-rich compounds is clearly indicated by a small excitonic peak present in the later compounds, which signifies the strong excitonic effects present in the Cl-rich system. The difference in the energy of the first bright excitation peak calculated from G_0W_0 and G_0W_0 +BSE spectra is used to estimate the exciton binding energy (see Table S7 within the Supplemental Material [41]). The difference in energy thus indicates that excitonic effects resolve the discrepancy between experimental and fundamental band gap simulated using the hybrid HSE06 functional as well. Using the G_0W_0 +BSE absorption spectra, SLME (spectroscopic limited maximum efficiency) versus film thickness were calculated, as shown in Fig. 5(b). SLME determines the maximum theoretical limit of the solar power-conversion efficiency of any absorber material. This is an improved

version of the Shockley and Queisser (SQ) efficiency. Along with the high absorption coefficients and suitable optical direct band gap, $\text{Cs}_2\text{Pt}(\text{Cl}_{0.04}\text{I}_{0.96})_6$ exhibits promising SLME. Coupled with a good optical response, the $\text{Cs}_2\text{Pt}(\text{Cl}_{0.04}\text{I}_{0.96})_6$ can be a good photoanode for PEC water oxidation, while the $\text{Cs}_2\text{Pt}(\text{Cl}_{0.96}\text{I}_{0.04})_6$ can be a prospective photocatalyst optimal for the overall water splitting, owing to its large band gap.

To explore the potential of the proposed mixed-halide perovskites for photo(electro)catalysis, it is paramount to benchmark their performance by calculating the fundamental descriptors—the absolute VBM and CBM energy levels (E_{VBM} and E_{CBM}) with respect to an external vacuum level. Band-edge potentials of pristine (Cs_2PtI_6 and Cs_2PtCl_6) and two prospective mixed-halide systems $\text{Cs}_2\text{Pt}(\text{Cl}_{0.04}\text{I}_{0.96})_6$ and $\text{Cs}_2\text{Pt}(\text{Cl}_{0.96}\text{I}_{0.04})_6$ calculated using the SCAN functional are presented in Fig. 5(c) with respect to vacuum and standard hydrogen electrode (SHE) scale. The valence-band edge of Cs_2PtI_6 is less positive than the water oxidation potential by 0.04 V. However, experimentally, Cs_2PtI_6 has been reported to be a functional photoanode for the oxygen evolution reaction [22]. The valence-band-edge potential simulated using the SCAN functional is in accordance with the experimental work by Jayaraman *et al.* [22]. This inconsistency in the simulated band edge position can also be attributed to the underestimated SCAN band gap of Cs_2PtI_6 (0.93 eV) in contrast to experimental value (1.25–1.43 eV). We have also calculated the band-edge positions using HSE06 functional and compared with those simulated using the SCAN functional. This is shown in Fig. S5 within the Supplemental Material [41]. Using the HSE functional, VBM of Cs_2PtI_6 fully traverses the oxidation potential for the oxygen-evolution reaction. The band edges of Cs_2PtCl_6 calculated herein are in accordance with the experimental findings [42], confirming its suitability

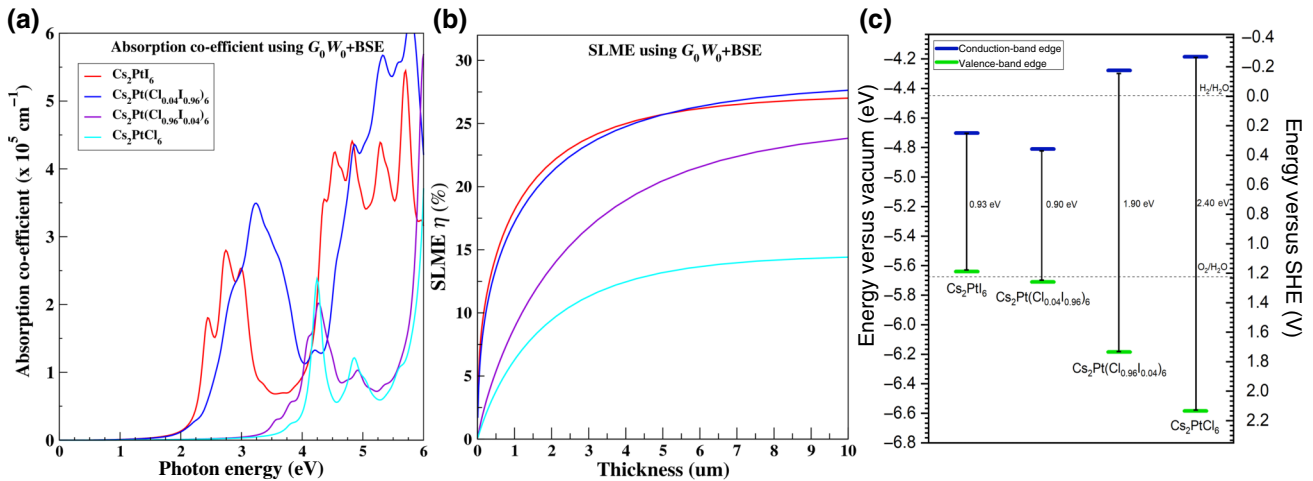


FIG. 5. (a) Absorption coefficients and corresponding (b) SLME versus film thickness for Cs_2PtI_6 , $\text{Cs}_2\text{Pt}(\text{Cl}_{0.04}\text{I}_{0.96})_6$, $\text{Cs}_2\text{Pt}(\text{Cl}_{0.96}\text{I}_{0.04})_6$, and Cs_2PtCl_6 simulated using G_0W_0 +BSE. (c) Band edge potentials of Cs_2PtI_6 , $\text{Cs}_2\text{Pt}(\text{Cl}_{0.04}\text{I}_{0.96})_6$, $\text{Cs}_2\text{Pt}(\text{Cl}_{0.96}\text{I}_{0.04})_6$, and Cs_2PtCl_6 .

for the overall water-splitting reaction. Furthermore, the mixed-halide system— $\text{Cs}_2\text{Pt}(\text{Cl}_{0.04}\text{I}_{0.96})_6$ —has VBM positioned 0.07 V more positive than the VBM position for Cs_2PtI_6 , based on both SCAN and HSE, indicating it is an alternative oxygen evolution reaction photo(electro)catalyst instead of Cs_2PtI_6 . In agreement with the HSE06 simulated band-edge potentials for all the systems (Fig. S5 within the Supplemental Material [41]), mixed-halide $\text{Cs}_2\text{Pt}(\text{Cl}_{0.04}\text{I}_{0.96})_6$ system has better valence-band alignment than the chloride-free counterpart. As such, replacement of Cs_2PtI_6 by $\text{Cs}_2\text{Pt}(\text{Cl}_{0.04}\text{I}_{0.96})_6$, followed by a creation of a heterojunction with electron- or hole-accepting semiconductors can improve the extraction of the photogenerated charge carriers. The band-edge potentials of $\text{Cs}_2\text{Pt}(\text{Cl}_{0.96}\text{I}_{0.04})_6$ straddle the hydrogen and oxygen evolution reaction redox potentials by 0.17 and 0.51 V, respectively. The findings above motivated us to explore the water resistance of the presented prospective mixed-halide systems, as discussed in the next section.

D. Stability against moisture (reaction with water)

The interaction of the environment with the surface of the target system plays a crucial role in the material stability. Thus, understanding the electronic properties and surface reconstruction of clean surface and H_2O -adsorbed surface provides useful insights into the chemical stability against water and, hence, guides how to model (I,Cl) mixed-halide systems to get optimal stability results. In addition, Bader charge analysis at or near the surface sheds light on the charge-transfer effects and its impact on stability.

Amongst the various stoichiometric and off-stoichiometric surfaces simulated [Fig. S7(a) within the Supplemental Material [41]], the (111) surface with the CsI_3 termination shows the lowest surface energy and is thus the most stable surface for Cs_2PtI_6 . Similarly, for Cs_2PtCl_6 [Fig. S7(b) within the Supplemental Material [41]], the stoichiometric (111) surface with CsCl_3 termination shows the lowest surface energy. The stable (111) CsCl_3 surface for Cs_2PtCl_6 and the (111) CsI_3 surface for Cs_2PtI_6 were further considered to study the H_2O adsorption effect on pure systems. The adsorption sites available on the (111)- CsCl_3 -terminal surface are Cs and Cl atom, with which either O or H atom of H_2O molecule can interact. Out of the four possible interfacial configurations (Cs—O, Cl—O, Cs—H, Cl—H), Cs—O with the oxygen atom of the H_2O molecule binding to the Cs atom on the surface turns out to be energetically the most stable one [see Fig. S10(b) within the Supplemental Material [41]]. Similarly, in case of Cs_2PtI_6 , the most preferred site for H_2O adsorption is the Cs atom making a bond with the O atom of H_2O [see Fig. S10(a) within the Supplemental Material [41]]. The adsorption energies of

H_2O on the (111)- CsCl_3 surface for Cs_2PtCl_6 and (111)- CsI_3 surface for Cs_2PtI_6 were calculated to be -0.22 and -0.47 eV, respectively. This indicates that the Cs_2PtI_6 is more hydrophilic as compared to Cs_2PtCl_6 . In comparison to adsorption energies of single perovskite CsSnCl_3 and VODP Cs_2SnCl_6 (reported as -0.93 and -0.60 eV [58]), the Cs_2PtCl_6 system is the least hydrophilic. In addition, Cs_2PtI_6 shows proportionately higher water stability as compared to Cs_2SnCl_6 . This manifests that selection of both halogen site as well B-cation sites can significantly alter the stability of the system. Figure 6(i) shows the H_2O adsorption energies of Cs_2PtI_6 , $\text{Cs}_2\text{Pt}(\text{Cl}_{0.04}\text{I}_{0.96})_6$, $\text{Cs}_2\text{Pt}(\text{Cl}_{0.96}\text{I}_{0.04})_6$, and Cs_2PtCl_6 in comparison to the state of the art materials—LHPs and other Sn-based single and VODP [65–70]. Clearly, Pt-based VODPs are more resistant to the H_2O adsorption and hence more stable in a water-rich environment.

The nature of chemical bonding on the surface plays a crucial role in dictating the adsorption energy and thus water stability. To understand the origin of stability at microscopic level, the bond length and charge distribution of the atoms on the surface were examined. For the (111)- CsCl_3 surface of Cs_2PtCl_6 , the adsorbed H_2O is located on the top of the Cs atom. The Cs—O bond length from the theoretically optimized structure is 3.15 Å. In the case of (111)- CsI_3 surface of Cs_2PtI_6 , the adsorbed H_2O is also located above the Cs atom. The Cs—O bond length in this case is 3.07 Å. The Cs—O bond in $\text{Cs}_2\text{PtI}_6/\text{H}_2\text{O}$ is relatively stronger than that in $\text{Cs}_2\text{PtCl}_6/\text{H}_2\text{O}$. This can also be confirmed from the Bader charge analysis. Table II shows a comparison of the Bader charges on surface atoms for clean surface and the H_2O adsorbed surface. It is evident that the transfer of charges from Cs to O is more prominent in the case of the $\text{Cs}_2\text{PtI}_6/\text{H}_2\text{O}$ system. The difference in the H_2O resistance strength of Cs_2PtCl_6 and Cs_2PtI_6 can be attributed to the bond strength of the Cs—Cl and Cs—I bonds, respectively, after and before the H_2O adsorption. For clean surfaces, the Cs—Cl bond is stronger than the Cs—I bond due to the smaller electronegativity difference, as well as smaller ionic radii of the Cl^- ion. The Cs_2PtI_6 has Cs—I dangling bonds on the surface, which may hinder its H_2O resistance ability. Whereas, the stronger Cs—Cl bonds impart stability to Cs_2PtCl_6 and remain unaffected upon encountering any foreign molecule. Additionally, upon adsorption of H_2O on the Cs atom, the bond lengths of the Cs atom with neighboring halide atoms get influenced significantly. In the case of Cs_2PtCl_6 , the Cs—Cl bond length increases by 0.01 Å after H_2O is adsorbed, whereas in Cs_2PtI_6 the Cs—I bond length increases by 0.14 Å. The weakening of the Cs—I bond, and strengthening of Cs—O bond in $\text{Cs}_2\text{PtI}_6/\text{H}_2\text{O}$ makes the system more hydrophilic. In contrast, for $\text{Cs}_2\text{PtCl}_6/\text{H}_2\text{O}$, the stronger Cs—Cl bond and the weaker Cs—O bond manifests the excellent water resistance ability of Cs_2PtCl_6 .

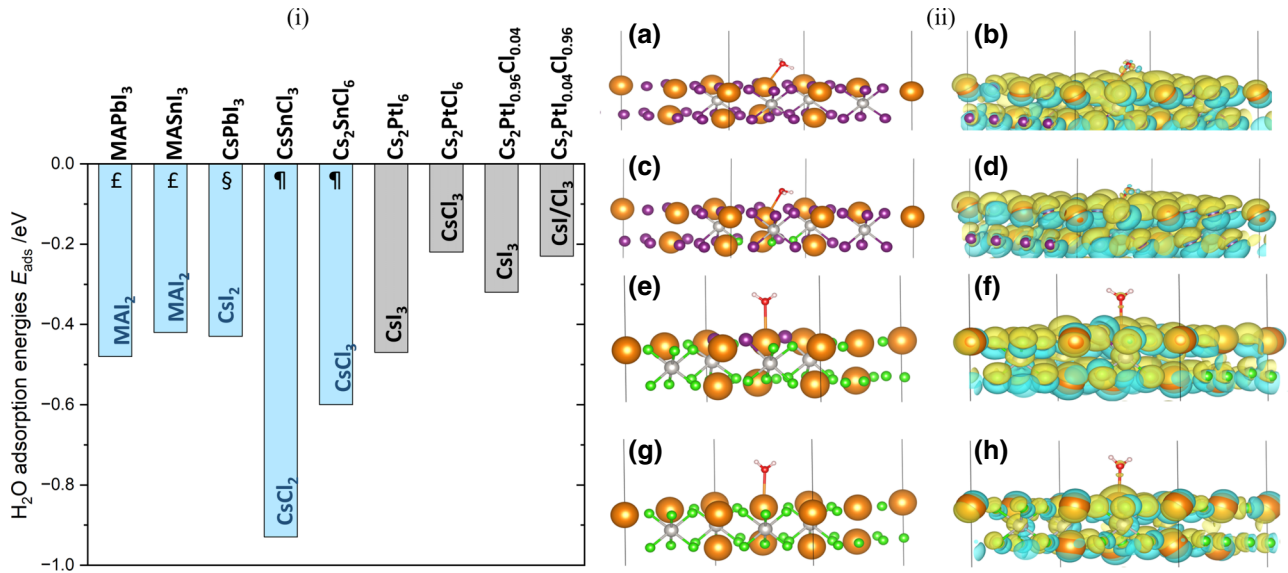


FIG. 6. (i) H₂O adsorption energies for different variants of perovskites. Ref: [65], §-[66], ¶-[58] (ii) (111) stable surface slabs (left) and charge-density difference plots (right) for Cs₂PtI₆/H₂O [Fig. (a),(b)], Cs₂PtCl₆/H₂O [Fig. (c),(d)], Cs₂Pt(Cl_{0.04}I_{0.96})₆/H₂O [Fig. (e),(f)], and Cs₂Pt(Cl_{0.96}I_{0.04})₆/H₂O [Fig. (g),(h)] systems. Cs, Pt, I, Cl, H, O atoms are represented by orange, grey, purple, green, peach, and red colors, respectively. Isosurfaces are displayed using yellow and cyan colours. Yellow represents positive electronic densities, which accept electrons (i.e., charge gain) and cyan represents negative densities, which donate electrons (i.e., charge loss) during chemical bonding.

Correspondingly, the H₂O adsorption energy of mixed-halide compounds—Cs₂Pt(Cl_{0.04}I_{0.96})₆ and Cs₂Pt(Cl_{0.96}I_{0.04})₆ were simulated for the (111) slab plane. For each of the systems, three configurations were considered—wherein the substituted halide atoms lie (a) on top layer (b) in intermediate layer and (c) in the middle layer (see Figs. S8 and S9 within the Supplemental Material [41]). The most stable surface termination of the Cs₂Pt(Cl_{0.04}I_{0.96})₆ system is when chlorine atoms lie in the intermediate layer and the top layer has all iodine atoms. This is in accordance with the surface energy of pristine systems, which signifies that surface energy of Cs₂PtI₆ is lower as compared to Cs₂PtCl₆ and hence iodine atoms preferentially reside on the top layer in the mixed-halide system. In view of the foregoing, the Cs₂Pt(Cl_{0.96}I_{0.04})₆ system theoretically stabilizes into its most stable configuration with iodine atoms nesting on the top layer. The adsorption energies of these two systems

Cs₂Pt(Cl_{0.04}I_{0.96})₆ and Cs₂Pt(Cl_{0.96}I_{0.04})₆ were simulated to be -0.31 and -0.23 eV, respectively. As compared to Cs₂PtCl₆, a remarkable enhancement in the water resistance with insertion of 4 at. % Cl into Cs₂PtI₆ is startling, despite the top surface of Cs₂Pt(Cl_{0.04}I_{0.96})₆ being entirely enclosed by Cs-I atoms and Cl atoms residing slightly deeper in the slab.

The impetus behind this can possibly be attributed to the difference in the charge transfer between the O of H₂O and the Cs on the exposed surface in case of Cs₂Pt(Cl_{0.04}I_{0.96})₆ and Cs₂Pt(Cl_{0.96}I_{0.04})₆. Figure 6(ii)(a),(c),(e),(g) and (b),(d),(f),(h) shows optimized structures and charge-density difference (CDD) diagrams for Cs₂PtI₆/H₂O, Cs₂Pt(Cl_{0.04}I_{0.96})₆/H₂O, Cs₂Pt(Cl_{0.96}I_{0.04})₆/H₂O, and Cs₂PtCl₆/H₂O systems, respectively. Isosurfaces are indicated using yellow and cyan color. Positive CDD (yellow region) represents charge gain and a negative CDD (cyan region) indicates loss of electric

TABLE II. Bader charge analysis of pristine Cs₂PtX₆ (X = Cl, I) and mixed-halide Cs₂Pt(Cl_xI_{1-x})₆ systems.

System	Bond length (in Å) Before H ₂ O adsorption	Bond length (in Å) After H ₂ O adsorption	Change of Bader charge Δq (e) upon adsorption of H ₂ O
Cs ₂ PtI ₆	Cs—I=4.15	Cs—O=3.07, Cs—I=4.29	Cs=+0.019, O=-1.260
Cs ₂ Pt(Cl _{0.04} I _{0.96}) ₆	Cs—I=4.17	Cs—O=3.08, Cs—I=4.20	Cs=+0.010, O=-1.217
	Cs—Cl=4.17	Cs—Cl=3.67	
Cs ₂ Pt(Cl _{0.96} I _{0.04}) ₆	Cs—I=3.61	Cs—O=3.18, Cs—I=3.70	Cs=+0.036, O=-1.211
	Cs—Cl=3.61	Cs—Cl=3.66	
Cs ₂ PtCl ₆	Cs—Cl=3.62	Cs—O=3.07, Cs—Cl=3.63	Cs=+0.006, O=-1.198

charge. The positive CDD (charge gain zone) is observed in the interface region between adsorbent host system and adsorbate- H_2O molecule, thus signifying the bonding between two surfaces. The extent of the charge gain region varies with the degree of adhesion energy of the H_2O molecule to the surface adsorption site at the interfacial system. As seen from Fig. 6(ii)(b), a major charge gain region is observed for $\text{Cs}_2\text{PtI}_6/\text{H}_2\text{O}$ system, which signifies stronger adhesion of H_2O to Cs_2PtI_6 making it more reactive to H_2O , and hence has lower water resistance. Comparatively, $\text{Cs}_2\text{PtCl}_6/\text{H}_2\text{O}$ system has smaller charge gain zone Fig. 6(ii)-(d) in the interface region, hence has improved stability against reaction with water.

Likewise, $\text{Cs}_2\text{Pt}(\text{Cl}_{0.96}\text{I}_{0.04})_6/\text{H}_2\text{O}$ also shows a CDD similar to $\text{Cs}_2\text{PtCl}_6/\text{H}_2\text{O}$. Hence it has H_2O adsorption energy closer to the Cl^- enriched pristine system. The CDD plot for $\text{Cs}_2\text{Pt}(\text{Cl}_{0.04}\text{I}_{0.96})_6/\text{H}_2\text{O}$ is similar to $\text{Cs}_2\text{PtI}_6/\text{H}_2\text{O}$ except that the extent of charge gain region is comparatively reduced. The smaller electronic densities in the interfacial region demonstrate the weakened interaction of H_2O with the $\text{Cs}_2\text{Pt}(\text{Cl}_{0.04}\text{I}_{0.96})_6$ system. The Bader charges and bond length results are in accordance to substantiate the CDD analysis claim. The presence of a small amount of Cl in $\text{Cs}_2\text{Pt}(\text{Cl}_{0.04}\text{I}_{0.96})_6$ helps to enhance the Cs—I bond on the surface as compared to pristine Cs_2PtI_6 , thus acting as a shield to protect the degradation of the system in the presence of H_2O .

IV. CONCLUSION

The prime motivation of this work was to address the bottleneck issue of moisture degradation faced by lead halide perovskites (LHP) and lead-free Sn-based perovskites, by considering Cs_2PtX_6 as alternative perovskite materials that can also exhibit excellent optoelectronic performance. Our chemical phase stability and optoelectronic study on a series of mixed-halide ($X = \text{I}, \text{Cl}$) compositions reveal the formation of a single homogeneous phase for $\text{Cs}_2\text{Pt}(\text{Cl}_x\text{I}_{1-x})_6$ with $x \leq 12$ at. % and $x \geq 92$ at. %. In contrast, $\text{Cs}_2\text{Pt}(\text{Cl}_x\text{I}_{1-x})_6$ with $x = 25$ at. %, 50 at. %, 75 at. %, and 88 at. % are found to co-exist in multiple phases with other secondary compounds. Identification of such secondary phases in our study is extremely useful to carefully tune the growth condition (during the synthesis) in such a way to avoid the phase segregation or multiple phase formation. We further explore the band gap versus x in $\text{Cs}_2\text{Pt}(\text{Cl}_x\text{I}_{1-x})_6$ to show an anomalous band-bowing behavior. This has been attributed to the symmetry-allowed transition in the mixed-halide case for $x = 8$ at. %, 12 at. %, 25 at. % (as compared to the pristine systems) and/or the formation of multiple phase formation in the intermediate ($x = 25$ at. %, 50 at. %, 75 at. %, and 88 at. %) Cl concentrations. Amongst the various mixed-halide phases, $\text{Cs}_2\text{Pt}(\text{Cl}_{0.04}\text{I}_{0.96})_6$ exhibits a reasonably good optical response, appreciable SLME

(spectroscopic limited maximum efficiency), appropriate band edges for PEC water oxidation and is coupled with excellent water resistance as compared to other LHPs and Sn-based perovskites. The $\text{Cs}_2\text{Pt}(\text{Cl}_{0.04}\text{I}_{0.96})_6$ system thus demonstrates the potential to be a good photoanode accompanied by enhanced water stability. Pt plays a crucial role in enhancing water resistance capability as well as optoelectronic properties when compared to other lead-free halide perovskites. This unarguably leaves a trail towards an unexplored path to perceive the genesis behind excellence of the Pt cation in $\text{Cs}_2\text{Pt}(\text{Cl}_x\text{I}_{1-x})_6$ that imparts remarkable solar absorption properties as well as stability against H_2O degradation.

ACKNOWLEDGMENTS

A.A. acknowledges computing facility (spacetime2) provided by IIT Bombay to support this research. A.N.S acknowledges the financial support from the Australian Research Council through a Future Fellowship (FT200100317). J.J. acknowledges financially the Australia Research Council funded Centre of Excellence in Exciton Science (Grant No. CE170100026). S.S.P. acknowledges the computational support by MASSIVE HPC facility (www.massive.org.au) and the Monash eResearch Centre and eSolutions-Research Support Services through the use of the MonARCH HPC Cluster.

- [1] Jason J. Yoo, Gabkyung Seo, Matthew R. Chua, Tae Gwan Park, Yongli Lu, Fabian Rotermund, Young-Ki Kim, Chan Su Moon, Nam Joong Jeon, and Juan-Pablo Correa-Baena *et al.*, Efficient perovskite solar cells via improved carrier management, *Nature* **590**, 587 (2021).
- [2] Jonas Kern, Johannes Heitmann, and Matthias Müller, Importance of the buffer layer properties for the performance of perovskite/silicon tandem solar cells, *ACS Appl. Energy Mater.* **6**, 2199 (2023).
- [3] Weijun Ke and Mercouri G. Kanatzidis, Prospects for low-toxicity lead-free perovskite solar cells, *Nat. Commun.* **10**, 965 (2019).
- [4] Xiaofeng Qiu, Bingqiang Cao, Shuai Yuan, Xiangfeng Chen, Zhiwen Qiu, Yanan Jiang, Qian Ye, Hongqiang Wang, Haibo Zeng, and Jian Liu *et al.*, From unstable CsSnI_3 to air-stable Cs_2SnI_6 : A lead-free perovskite solar cell light absorber with bandgap of 1.48 eV and high absorption coefficient, *Solar Energy Mater. Solar Cells* **159**, 227 (2017).
- [5] Anna Abfalterer, Javad Shamsi, Dominik J. Kubicki, Christopher N. Savory, James Xiao, Giorgio Divitini, Weiwei Li, Stuart Macpherson, Krzysztof Gałkowski, and Judith L. MacManus-Driscoll *et al.*, Colloidal synthesis and optical properties of perovskite-inspired cesium zirconium halide nanocrystals, *CS Mater. Lett.* **2**, 1644 (2020).
- [6] Keiichiro Saeki, Yuki Wakai, Yutaka Fujimoto, Masanori Koshimizu, Takayuki Yanagida, Daisuke Nakauchi, and

- Keisuke Asai, Luminescence and scintillation properties of Rb_2HfCl_6 crystals, *Jpn. J. Appl. Phys.* **55**, 110311 (2016).
- [7] Arnold Burger, Emmanuel Rowe, Michael Groza, Kristle Morales Figueroa, Nerine J. Cherepy, Patrick R. Beck, Steven Hunter, and Stephen A. Payne, Cesium hafnium chloride: A high light yield, non-hygroscopic cubic crystal scintillator for gamma spectroscopy, *Appl. Phys. Lett.* **107**, 143505 (2015).
- [8] Rehan Ullah, Malak Azmat Ali, Afzal Khan, G. Murtaza, Asif Mahmood, and Shahid M. Ramay, Influence of the spin-orbit coupling effect on the electronic and thermoelectric properties of Cs_2MI_6 ($\text{M} = \text{Zr, Hf}$) variant perovskites, *Mater. Res. Bull.* **134**, 111112 (2021).
- [9] Tong Chang, Qilin Wei, Ruosheng Zeng, Sheng Cao, Jialong Zhao, and Bingsuo Zou, Efficient energy transfer in Te^{4+} -doped Cs_2ZrCl_6 vacancy-ordered perovskites and ultrahigh moisture stability via a-site rb-alloying strategy, *J. Phys. Chem. Lett.* **12**, 1829 (2021).
- [10] Jun Zhou, Ximing Rong, Maxim S Molokeev, Yulong Wang, Xiangyan Yun, Denghui Xu, and Xiong Li, Alloying Cs^+ into Rb_2ZrCl_6 Te^{4+} toward highly efficient and stable perovskite variants, *Mater. Chem. Front.* **5**, 4997 (2021).
- [11] Noah P. Holzappel, Jackson D. Majher, T Amanda Strom, Curtis E. Moore, and Patrick M. Woodward, $\text{Cs}_4\text{Cd}_{1-x}\text{MnxBi}_2\text{Cl}_{12}$ vacancy-ordered halide perovskite phosphor with high-efficiency orange-red emission, *Chem. Mater.* **32**, 3510 (2020).
- [12] Zhifang Tan, Jinghui Li, Cheng Zhang, Zha Li, Qingsong Hu, Zewen Xiao, Toshio Kamiya, Hideo Hosono, Guangda Niu, and Efrat Lifshitz *et al.*, Highly efficient blue-emitting Bi-doped Cs_2SnCl_6 perovskite variant: Photoluminescence induced by impurity doping, *Adv. Funct. Mater.* **28**, 1801131 (2018).
- [13] Pengfei Cheng, Daoyuan Zheng, Lu Feng, Yuefeng Liu, Junxue Liu, Juntao Li, Yang Yang, Guoxiong Wang, and Keli Han, Doped all-inorganic cesium zirconium halide perovskites with high-efficiency and tunable emission, *J. Energy Chem.* **65**, 600 (2022).
- [14] Jinghui Li, Zhifang Tan, Manchen Hu, Chao Chen, Jiajun Luo, Shunran Li, Liang Gao, Zewen Xiao, Guangda Niu, and Jiang Tang, Antimony doped Cs_2SnCl_6 with bright and stable emission, *Front. Optoelectron.* **12**, 352 (2019).
- [15] Ruosheng Zeng, Kun Bai, Qilin Wei, Tong Chang, Jun Yan, Bao Ke, Jialuo Huang, Liushun Wang, Weichang Zhou, and Sheng Cao *et al.*, Boosting triplet self-trapped exciton emission in Te (IV)-doped Cs_2SnCl_6 perovskite variants, *Nano Res.* **14**, 1551 (2021).
- [16] Byunghong Lee, Anthony Krenselewski, Sung Il Baik, David N Seidman, and Robert P. H. Chang, Solution processing of air-stable molecular semiconducting iodosalts, $\text{Cs}_2\text{SnI}_{6-x}\text{Br}_x$, for potential solar cell applications, *Sustainable Energy Fuels* **1**, 710 (2017).
- [17] Min Chen, Ming-Gang Ju, Alexander D. Carl, Yingxia Zong, Ronald L. Grimm, Jiajun Gu, Xiao Cheng Zeng, Yuanyuan Zhou, and Nitin P. Padture, Cesium titanium (iv) bromide thin films based stable lead-free perovskite solar cells, *Joule* **2**, 558 (2018).
- [18] Byunghong Lee, Yamuna Ezhumalai, Woongkyu Lee, Ming-Chou Chen, Chen-Yu Yeh, Tobin J Marks, and Robert P. H. Chang, Cs_2SnI_6 -encapsulated multidy-
- sensitized all-solid-state solar cells, *ACS Appl. Mater. Interfaces* **11**, 21424 (2019).
- [19] Dakota Schwartz, Rubaiya Murshed, Harry Larson, Benedikt Usprung, Sina Soltanmohamad, Ramesh Pandey, Edward S. Barnard, Angus Rockett, Thomas Hartmann, and Ivano E. Castelli *et al.*, Air stable, high-efficiency, Pt-based halide perovskite solar cells with long carrier lifetimes, *Physica Status Solidi (RRL)–Rapid Research Letters* **14**, 2000182 (2020).
- [20] Curtis Walkons, Rubaiya Murshed, and Shubhra Bansal, Numerical analysis of Pb-free perovskite absorber materials: Prospects and challenges, *Solar RRL* **4**, 2000299 (2020).
- [21] Muhammed Hamdan and Aravind Kumar Chandiran, Cs_2PtI_6 halide perovskite is stable to air, moisture, and extreme pH: Application to photoelectrochemical solar water oxidation, *Angew. Chem.* **59**, 16033 (2020).
- [22] Jayanthan P. Jayaraman, Muhammed Hamdan, Manishankar Velpula, Niket S. Kaisare, and Aravind Kumar Chandiran, $\text{BiVO}_4/\text{Cs}_2\text{PtI}_6$ vacancy-ordered halide perovskite heterojunction for panchromatic light harvesting and enhanced charge separation in photoelectrochemical water oxidation, *ACS Appl. Mater. Interfaces* **13**, 16267 (2021).
- [23] Shuzhang Yang, Liang Wang, Shuai Zhao, Anmin Liu, Yi Zhou, Qianji Han, Fengyang Yu, Liguang Gao, Chu Zhang, and Tingli Ma, Novel lead-free material Cs_2PtI_6 with narrow bandgap and ultra-stability for its photovoltaic application, *ACS Appl. Mater. Interfaces* **12**, 44700 (2020).
- [24] Zhifang Tan, Yanmeng Chu, Jinxi Chen, Jinghui Li, Guoqi Ji, Guangda Niu, Liang Gao, Zewen Xiao, and Jiang Tang, Lead-free perovskite variant solid solutions $\text{Cs}_2\text{Sn}_{1-x}\text{Te}_x\text{Cl}_6$: Bright luminescence and high anti-water stability, *Adv. Mater.* **32**, 2002443 (2020).
- [25] Jackson D. Majher, Matthew B. Gray, T. Amanda Strom, and Patrick M. Woodward, $\text{Cs}_2\text{NaBiCl}_6$: Mn^{2+} – A new orange-red halide double perovskite phosphor, *Chem. Mater.* **31**, 1738 (2019).
- [26] Zhilin Li, Zhihui Rao, Qiaoqiao Li, Liujiang Zhou, Xiujian Zhao, and Xiao Gong, $\text{Cs}_2\text{Zr}_{1-x}\text{Te}_x\text{Cl}_6$ perovskite microcrystals with ultrahigh photoluminescence quantum efficiency of 79.46% for high light efficiency white light emitting diodes, *Adv. Opt. Mater.* **9**, 2100804 (2021).
- [27] Ruxin Liu, Wenjun Zhang, Wenjing Liu, and Guojing Li, Synthesis of a Bi^{3+} -doped Cs_2HfCl_6 double perovskite with highly efficient blue light emission at room temperature, *Inorg. Chem.* **60**, 10451 (2021).
- [28] Annalise E. Maughan, Alex M. Ganose, Mitchell M. Bordelon, Elisa M. Miller, David O. Scanlon, and James R. Neilson, Defect tolerance to intolerance in the vacancy-ordered double perovskite semiconductors Cs_2SnI_6 and Cs_2TeI_6 , *J. Am. Chem. Soc.* **138**, 8453 (2016).
- [29] Hadeer H. AbdElAziz, Mohamed Taha, Waleed M. A. El Roubay, M. H. Khedr, and Laila Saad, Evaluating the performance of $\text{Cs}_2\text{PtI}_{6-x}\text{Br}_x$ for photovoltaic and photocatalytic applications using first-principles study and scaps-1d simulation, *Heliyon* **8**, e10808 (2022).

- [30] Hang Yin, Junsheng Chen, Peng Guan, Daoyuan Zheng, Qingkun Kong, Songqiu Yang, Panwang Zhou, Bin Yang, Tönü Pullerits, and Keli Han, Controlling photoluminescence and photocatalysis activities in lead-free $\text{Cs}_2\text{Pt}_x\text{Sn}_{1-x}\text{Cl}_6$ perovskites via ion substitution, *Angew. Chem., Int. Ed.* **60**, 22693 (2021).
- [31] Akfeen Amjad, Samina Qamar, Chengchen Zhao, Kalsoom Fatima, Muhammad Sultan, and Zareen Akhter, Numerical simulation of lead-free vacancy ordered Cs_2PtI_6 based perovskite solar cell using SCAPS-1D, *RSC Adv.* **13**, 23211 (2023).
- [32] Santosh Bimli, Vishesh Manjunath, Sameena R. Mulani, Aayushi Miglani, Onkar S. Game, and Rupesh S. Devan, Theoretical investigations of all inorganic Cs_2SnI_6 double perovskite solar cells for efficiency 30%, *Solar Energy* **256**, 76 (2023).
- [33] Annalise E. Maughan, Alex M. Ganose, David O. Scanlon, and James R. Neilson, Perspectives and design principles of vacancy-ordered double perovskite halide semiconductors, *Chem. Mater.* **31**, 1184 (2019).
- [34] Weiguang Zhu, Tiankai Yao, Junhua Shen, Wenqian Xu, Bowen Gong, Yachun Wang, and Jie Lian, In situ investigation of water interaction with lead-free all inorganic perovskite $\text{Cs}_2\text{SnI}_x\text{Cl}_{6-x}$, *J. Phys. Chem. C* **123**, 9575 (2019).
- [35] Zi-Yan Wang, Yi Chen, Chongyang Zhang, Dan Wang, Pei Liang, Hong Zhang, Rong-Jun Xie, and Le Wang, Electronic structure and optical properties of vacancy-ordered double perovskites $\text{Cs}_2\text{PdBr}_x\text{Cl}_{6-x}$ by first-principles calculation, *J. Phys. Chem. C* **124**, 13310 (2020).
- [36] Georg Kresse and Jürgen Hafner, Ab initio molecular dynamics for liquid metals, *Phys. Rev. B* **47**, 558 (1993).
- [37] Paulo V. C. Medeiros, Sven Stafström, and Jonas Björk, Effects of extrinsic and intrinsic perturbations on the electronic structure of graphene: Retaining an effective primitive cell band structure by band unfolding, *Phys. Rev. B* **89**, 041407 (2014).
- [38] Paulo V. C. Medeiros, Stepan S. Tsirkin, Sven Stafström, and Jonas Björk, Unfolding spinor wave functions and expectation values of general operators: Introducing the unfolding-density operator, *Phys. Rev. B* **91**, 041116 (2015).
- [39] Stefan Albrecht, Lucia Reining, Rodolfo Del Sole, and Giovanni Onida, Ab initio calculation of excitonic effects in the optical spectra of semiconductors, *Phys. Rev. Lett.* **80**, 4510 (1998).
- [40] Michael Rohlfing and Steven G. Louie, Electron-hole excitations in semiconductors and insulators, *Phys. Rev. Lett.* **81**, 2312 (1998).
- [41] See Supplemental Material at <http://link.aps.org/supplemental/10.1103/PhysRevApplied.21.044031> for further auxiliary details on computational methods, structural and phase chemical stability, band-gap sensitivity to exchange correlation functional, density of states, optical properties and exciton binding energies of mixed-halide compositions, chemical-bonding analysis, electronic band structure, dipole-dipole transition probability and more details on surface study for moisture stability.
- [42] Muhammed Hamdan, Manasa Manoj, Jigar Shaileshkumar Halpati, and Aravind Kumar Chandiran, Acid- and base-stable $\text{Cs}_2\text{Pt}(\text{Cl}, \text{Br})_6$ vacancy-ordered double perovskites and their core-shell heterostructures for solar water oxidation, *Solar RRL* **6**, 2101092 (2022).
- [43] Diethard Sinram, Brendel Claus, and Krebs Bernt, Hexa-iodoanions of titanium, zirconium, hafnium, palladium and platinum: Preparation, properties and crystal structures of the caesium salts, *Inorganica Chim. Acta* **131**, L131 (1982).
- [44] Muhammad Faizan, K. C. Bhamu, Ghulam Murtaza, Xin He, Neeraj Kulhari, Murefah Mana AL-Anazy, and Shah Haidar Khan, Electronic and optical properties of vacancy ordered double perovskites A_2BX_6 (A= Rb, Cs; B= Sn, Pd, Pt; and X= Cl, Br, I): A first principles study, *Sci. Rep.* **11**, 6965 (2021).
- [45] Ranyun Wu, Yingmeng Liu, Sanlue Hu, Pengfei Fu, and Zewen Xiao, Red-emitting perovskite variant Cs_2PtCl_6 phosphor: Material design, luminous mechanism, and application in high-color-rendering white light-emitting diodes, *Adv. Opt. Mater.* **10**, 2201081 (2022).
- [46] John Buckeridge, David O. Scanlon, Aron Walsh, and C. Richard A. Catlow, Automated procedure to determine the thermodynamic stability of a material and the range of chemical potentials necessary for its formation relative to competing phases and compounds, *Comput. Phys. Commun.* **185**, 330 (2014).
- [47] Liping Yu and Alex Zunger, Identification of potential photovoltaic absorbers based on first-principles spectroscopic screening of materials, *Phys. Rev. Lett.* **108**, 068701 (2012).
- [48] N. Hatada, Software for creating chemical potential diagrams. *Chesta Code, Software for Creating Chemical Potential Diagrams.*
- [49] Graeme Henkelman, Andri Arnaldsson, and Hannes Jónsson, A fast and robust algorithm for Bader decomposition of charge density, *Comput. Mater. Sci.* **36**, 354 (2006).
- [50] Muhammad Sajjad, Qasim Mahmood, Nirpendra Singh, and J. Andreas Larsson, Ultralow lattice thermal conductivity in double perovskite Cs_2PtI_6 : A promising thermoelectric material, *ACS Appl. Energy Mater.* **3**, 11293 (2020).
- [51] John P. Perdew, Kieron Burke, and Matthias Ernzerhof, Generalized gradient approximation made simple, *Phys. Rev. Lett.* **77**, 3865 (1996).
- [52] G Bergerhoff, I. D. Brown, and F Allen *et al.*, Crystallographic databases, International Union of Crystallography, *Chester* **360**, 77 (1987).
- [53] Weiguang Zhu, Guoqing Xin, Yiping Wang, Xin Min, Tiankai Yao, Wenqian Xu, Minghao Fang, Sufei Shi, Jian Shi, and Jie Lian, Tunable optical properties and stability of lead free all inorganic perovskites $\text{Cs}_2\text{SnI}_x\text{Cl}_{6-x}$, *J. Mater. Chem. A* **6**, 2577 (2018).
- [54] Rongjian Sa, Qiqi Zhang, Benlong Luo, and Diwen Liu, Exploring the electronic and optical properties of vacancy-ordered double perovskites Cs_2PtX_6 (X= Cl, Br, I), *J. Solid State Chem.* **304**, 122602 (2021).
- [55] Yao Cai, Wei Xie, Hong Ding, Yan Chen, Krishnamoorthy Thirumal, Lydia H. Wong, Nripan Mathews, Subodh G. Mhaisalkar, Matthew Sherburne, and Mark Asta, Computational study of halide perovskite-derived A_2BX_6 inorganic compounds: Chemical trends in electronic structure and structural stability, *Chem. Mater.* **29**, 7740 (2017).

- [56] Jochen Heyd, Gustavo E. Scuseria, and Matthias Ernzerhof, Hybrid functionals based on a screened Coulomb potential, *J. Chem. Phys.* **118**, 8207 (2003).
- [57] Matthias Wuttig, Carl-Friedrich Schön, Mathias Schumacher, John Robertson, Pavlo Golub, Eric Bousquet, Carlo Gatti, and Jean-Yves Raty, Halide perovskites: Advanced photovoltaic materials empowered by a unique bonding mechanism, *Adv. Funct. Mater.* **32**, 2110166 (2022).
- [58] Yanmeng Chu, Yue Hu, and Zewen Xiao, First-principles insights into the stability difference between ABX_3 halide perovskites and their A_2BX_6 variants, *J. Phys. Chem. C* **125**, 9688 (2021).
- [59] Qiang Gao, Hasan Sahin, Jun Kang, and Su-Huai Wei, Origin of anomalous band-gap bowing in two-dimensional tin-lead mixed perovskite alloys, *Phys. Rev. B* **104**, 064204 (2021).
- [60] Maham M. S. Karim, Alex M. Ganose, Laura Pieters, W. W. Winnie Leung, Jessica Wade, Lina Zhang, David O. Scanlon, and Robert G. Palgrave, Anion distribution, structural distortion, and symmetry-driven optical band gap bowing in mixed halide Cs_2SnX_6 vacancy ordered double perovskites, *Chem. Mater.* **31**, 9430 (2019).
- [61] Anuj Goyal, Scott McKechnie, Dimitar Pashov, William Tumas, Mark Van Schilfgaarde, and Vladan Stevanovic, Origin of pronounced nonlinear band gap behavior in lead-tin hybrid perovskite alloys, *Chem. Mater.* **30**, 3920 (2018).
- [62] Chaiyawat Kaewmeechai, Yongyut Laosiritaworn, and Atchara Punya Jaroenjittichai, Dft calculation on electronic properties of vacancy-ordered double perovskites $Cs_2(Ti, Zr, Hf)X_6$ and their alloys: Potential as light absorbers in solar cells, *Results Phys.* **30**, 104875 (2021).
- [63] Yi-Teng Huang, Seán R. Kavanagh, David O Scanlon, Aron Walsh, and Robert L. Z. Hoye, Perovskite-inspired materials for photovoltaics and beyond—from design to devices, *Nanotechnology* **32**, 132004 (2021).
- [64] Seán R. Kavanagh, Christopher N. Savory, Shanti M. Liga, Gerasimos Konstantatos, Aron Walsh, and David O. Scanlon, Frenkel excitons in vacancy-ordered titanium halide perovskites Cs_2TiX_6 , *J. Phys. Chem. Lett.* **13**, 10965 (2022).
- [65] Waldemar Kaiser, Damiano Ricciarelli, Edoardo Mosconi, Asma A. Allothman, Francesco Ambrosio, and Filippo De Angelis, Stability of tin-versus lead-halide perovskites: Ab initio molecular dynamics simulations of perovskite/water interfaces, *J. Phys. Chem. Lett.* **13**, 2321 (2022).
- [66] Dhana Lakshmi Busipalli, Kuan-Yu Lin, Santhanamoorthi Nachimuthu, and Jyh-Chiang Jiang, Enhanced moisture stability of cesium lead iodide perovskite solar cells—A first-principles molecular dynamics study, *Phys. Chem. Chem. Phys.* **22**, 5693 (2020).
- [67] Sanjun Wang, Wen-bo Xiao, and Fei Wang, Structural, electronic, and optical properties of cubic formamidinium lead iodide perovskite: A first-principles investigation, *RSC Adv.* **10**, 32364 (2020).
- [68] Giacomo Giorgi, Jun-Ichi Fujisawa, Hiroshi Segawa, and Koichi Yamashita, Small photocarrier effective masses featuring ambipolar transport in methylammonium lead iodide perovskite: A density functional analysis, *J. Phys. Chem. Lett.* **4**, 4213 (2013).
- [69] Jing Feng and Bing Xiao, Effective masses and electronic and optical properties of nontoxic $MASnX_3$ ($X = Cl, Br, I$) perovskite structures as solar cell absorber: A theoretical study using HSE06, *J. Phys. Chem. C* **118**, 19655 (2014).
- [70] Qihua Li, Zehua Chen, Ionut Tranca, Silvia Gaastra-Nedea, David Smeulders, and Shuxia Tao, Compositional effect on water adsorption on metal halide perovskites, *Appl. Surf. Sci.* **538**, 148058 (2021).